

## Research Article

# Using $^{10}\text{Be}$ dating to determine when the Cordilleran Ice Sheet stopped flowing over the Canadian Rocky Mountains

Helen E. Dulfer<sup>a\*</sup> , Martin Margold<sup>a</sup> , Zbyněk Engel<sup>a</sup> , Régis Braucher<sup>b</sup>  and Aster Team<sup>b</sup>

<sup>a</sup>Department of Physical Geography and Geoecology, Faculty of Science, Charles University in Prague, Albertov 6, 12800 Praha, Czech Republic. and <sup>b</sup>CEREGE, Aix-Marseille Univ., CNRS-IRD- Coll. De France-INRAE UM 34, 13545 Aix-en-Provence Cedex 4, France Aster Team: Georges Aumaitre, Didier Bourlès, Karim Keddadouche

### Abstract

During the last glacial maximum the Cordilleran and Laurentide ice sheets coalesced east of the Rocky Mountains and geomorphological evidence indicates ice flowed over the main ridge of the Rocky Mountains between  $\sim 54\text{--}56^\circ\text{N}$ . However, this ice flow has thus far remained unconstrained in time. Here we use in situ produced cosmogenic  $^{10}\text{Be}$  dating to determine when Cordilleran ice stopped flowing over the mountain range. We dated eight samples from two sites: one on the western side (Mount Morfee) and one on the eastern side (Mount Spieker) of the Rocky Mountains. At Mount Spieker, one sample is rejected as an outlier and the remaining three give an apparent weighted mean exposure age of  $15.6 \pm 0.6$  ka. The four samples at Mount Morfee are well clustered in time and give an apparent weighted mean exposure age of  $12.2 \pm 0.4$  ka. These ages indicate that Mount Spieker became ice free before the Bølling warming and that the western front of the Rocky Mountains (Mount Morfee) remained in contact with the Cordilleran Ice Sheet until the Younger Dryas.

**Keywords:** Cordilleran Ice Sheet, Rocky Mountains, cosmogenic exposure dating, deglaciation

(Received 29 May 2020; accepted 4 December 2020)

### INTRODUCTION

The Cordilleran Ice Sheet (CIS) repeatedly covered the mountainous regions of western North America during the Pleistocene and formed part of the North American Ice Sheet Complex during the last glacial maximum (LGM). The CIS had an ice volume sea level equivalent of 7–9 m (Seguinot et al., 2016), which is similar to the present-day Greenland Ice Sheet. Recent studies indicate that the CIS underwent substantial ice mass loss during the Bølling warming, after which the last stage of deglaciation is largely unknown (Peltier et al., 2015; Lambeck et al., 2017; Menounos et al., 2017). This makes the CIS one of the least understood ephemeral Pleistocene ice sheets.

The interaction between the Cordilleran and Laurentide ice sheets east of the Rocky Mountains at the LGM has been debated for many decades, with some researchers arguing for the coalescence of the two ice sheets on the westernmost Interior Plains (e.g., Mathews, 1978; Dyke and Prest, 1987; Stumpf et al., 2000; Dyke et al., 2003; Dyke, 2004; Bednarski and Smith, 2007), while others argue that the CIS did not extend over the Rocky Mountains at the local LGM (LLGM) (e.g., Bobrowsky and Rutter, 1992; Catto et al., 1996). Recently, empirical evidence supporting the coalescence of the two ice sheets has grown (Atkinson et al., 2016; Hickin et al., 2016; Hartman et al., 2018), and it is now generally accepted that they coalesced at the LLGM (Fig. 1).

Recent studies based on glacial isostatic adjustment (GIA) analysis indicate substantial ice thickness in the area of coalescence, with an ice saddle connecting the dome areas of the two ice sheets (Peltier et al., 2015; Lambeck et al., 2017). However, the LLGM ice sheet configuration of the CIS is still not fully understood.

Empirical evidence indicates that ice flowed over the Rocky Mountains at the Hart Ranges (Fig. 2), the lowest and least rugged section of the mountain range (summits averaging 2300 m above sea level [asl]). This evidence includes (1) sets of attenuated bedforms on either side of the Hart Ranges, which record fast ice flow towards the Rocky Mountains (Prince George swarm; Kleman et al., 2010; Sacco et al., 2017) and fast ice flow radiating from the Rocky Mountain Foothills (Fig. 2; Prest et al., 1968; Kleman et al., 2010; Shaw et al., 2010; Atkinson et al., 2016; Hickin et al., 2016), (2) northeast-trending streamlined landforms on mountain summits between  $55^\circ\text{N}$  and  $56^\circ\text{N}$  (Fig. 3a), (3) geomorphological evidence of ice drainage through a system of broad mountain cols located between  $54.5^\circ\text{N}$  and  $55^\circ\text{N}$  (Fig. 3b), (4) eastwardly transported glacial erratics along the Rocky Mountain Foothills (Bednarski and Smith, 2007), and (5) the presence of volcanic-rich Cordilleran till east of the Rocky Mountains (Mathews, 1978; Bednarski and Smith, 2007; Hartman et al., 2018).

Margold et al. (2018, 2019) incorporated ice flow over the Hart Ranges into a broader, regional picture of the ice sheet configuration, showing the ice drainage pattern at, and shortly after, the LLGM. According to their reconstructions, which integrated data on the glacial geomorphology (Margold et al., 2015a, b) with information from glacial isostasy (Peltier, 2004; Peltier et al., 2015; Lambeck et al., 2017) and numerical ice sheet modelling (Tarasov and Peltier, 2004; Tarasov et al., 2012), an ice

\*Corresponding author: Helen E. Dulfer, Email: [dulferh@natur.cuni.cz](mailto:dulferh@natur.cuni.cz)

Cite this article: Dulfer HE, Margold M, Engel Zbyněk, Braucher R, Team A (2021). Using  $^{10}\text{Be}$  dating to determine when the Cordilleran Ice Sheet stopped flowing over the Canadian Rocky Mountains. *Quaternary Research* 102, 222–233. <https://doi.org/10.1017/qua.2020.122>

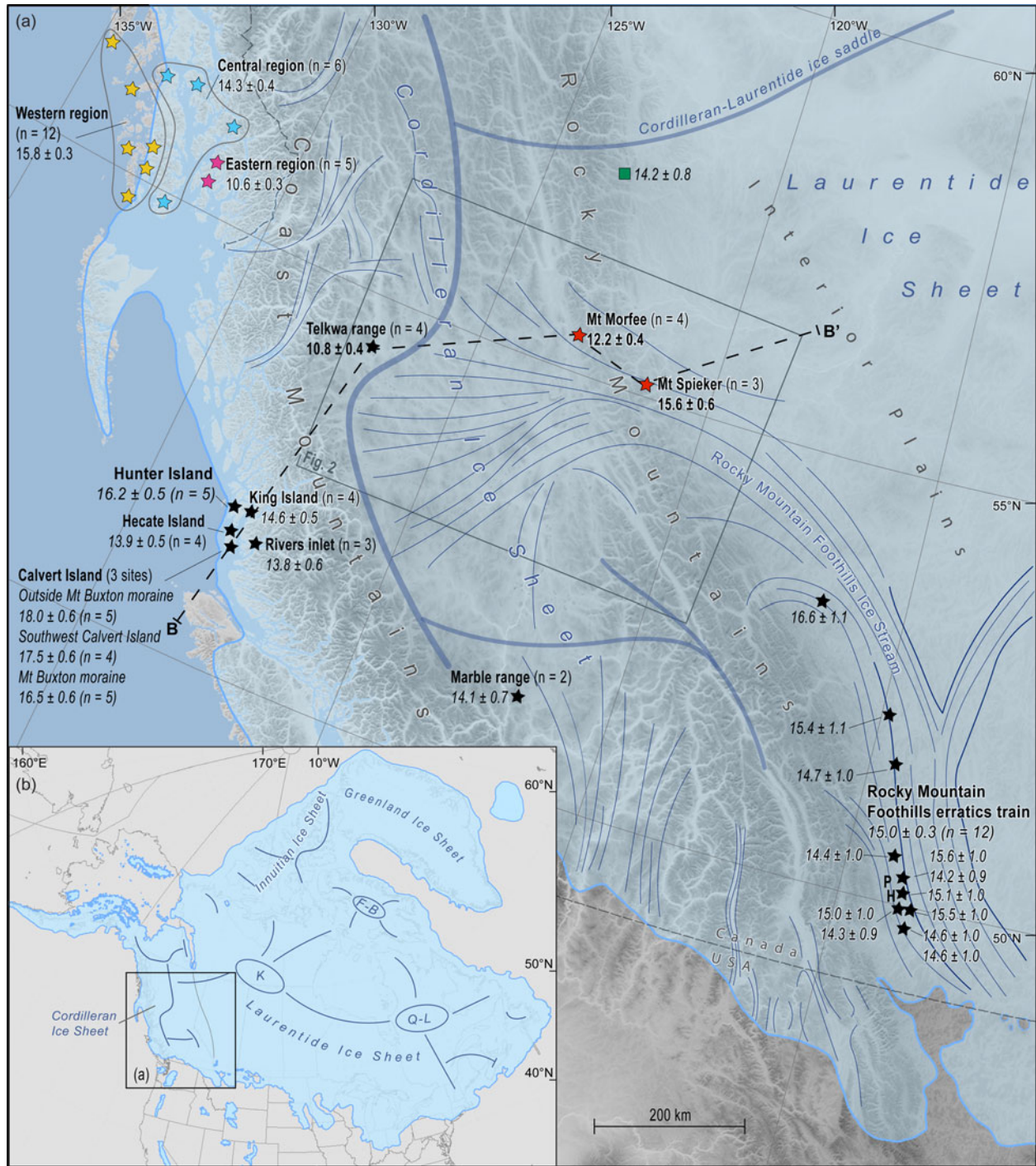


**Figure 1.** (a) Configuration of the Cordilleran Ice Sheet at 22.1 cal ka BP, based on Kleman et al. (2010), Margold et al. (2018, 2019), and Dalton et al. (2020). The approximate position of the ice divide at the ILGM is shown with thick blue lines; ice flow direction is indicated by thin blue lines. The locations of Mount Morfee and Mount Spieker are given by the red stars; remaining stars show the locations of selected <sup>10</sup>Be cosmogenic nuclide ages relating to the deglaciation of the CIS from Margold et al. (2014, 2019), Darvill et al. (2018), and Lesnek et al. (2018, 2020). All ages have been recalculated using the online calculator of Balco et al. (2008; version 3.0) and corrected for glacioisostatic rebound. The ages in bold also have been corrected for snow cover. All ages are given in thousands of years (ka) and are reported with a 1σ external error. In most cases the weighted mean age of a specific number of samples (n) is given. The green square gives the location of a <sup>36</sup>Cl exposure age from Bednarski and Smith (2007) that has not been recalculated. The abbreviation PH shows the location of the Porcupine Hills. The location of the transect shown in Fig. 8 is given by the black dashed line B–B'. (b) Inset map of the North American Ice Sheet Complex showing the location of the Cordilleran Ice Sheet and the ice extent at 22.1 cal ka BP. The approximate positions of the ice divides and ice domes are shown by the thick blue lines (K = Keewatin dome, Q-L = Québec-Labrador dome, F-B = Foxe-Baffin dome; Margold et al., 2018). (For interpretation of the references to color in this figure legend, the reader is referred to the web version of this article.)

saddle connecting the CIS and Laurentide Ice Sheet (LIS) was located east of the Rocky Mountains at the ILGM. Cordilleran ice flowed over the Rocky Mountains and into the Rocky

Mountain Foothills Ice Stream, a tributary of an anastomosing ice stream system draining the Keewatin ice dome of the LIS at the ILGM (Fig. 1).

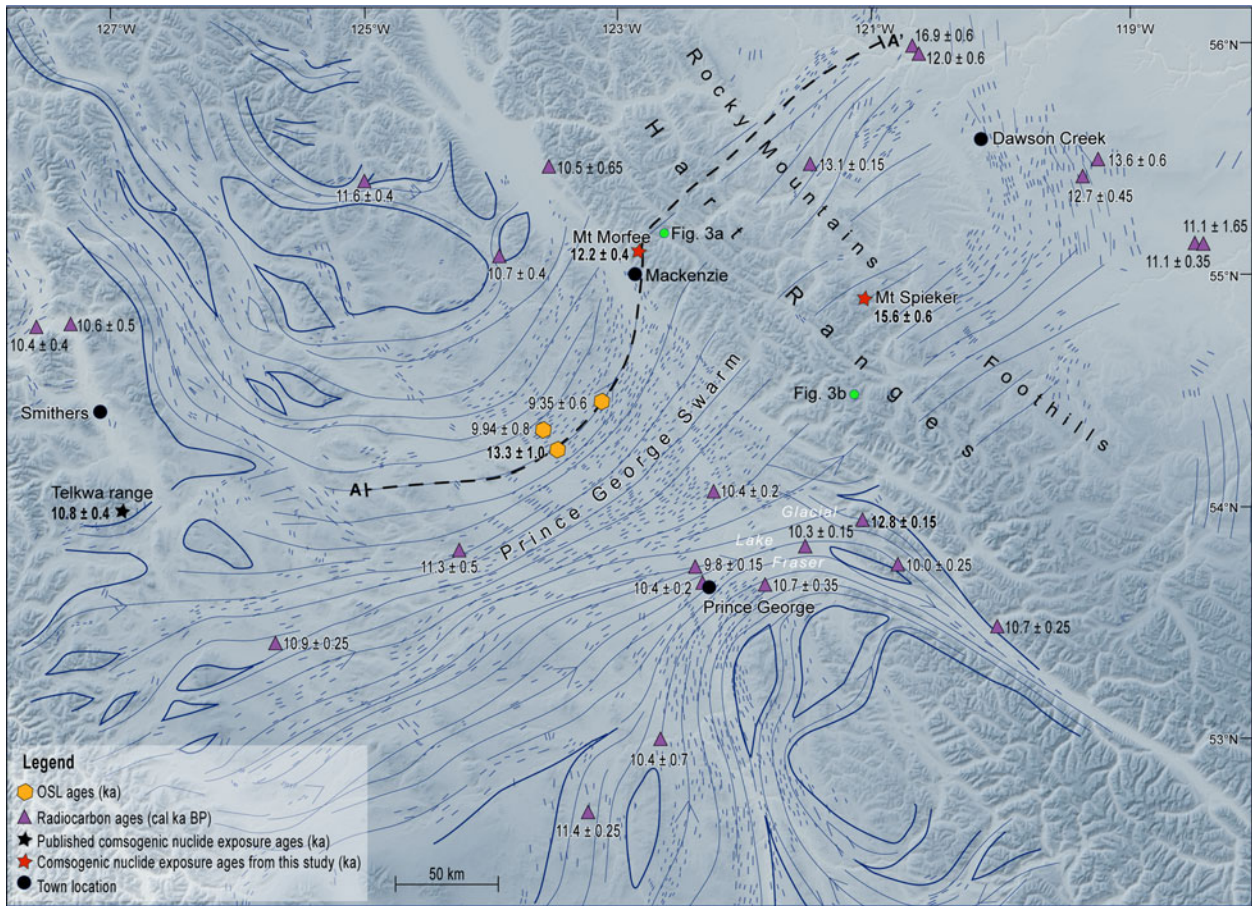


**Figure 2.** Regional map of the ice flow surrounding the Hart Ranges. The thin blue lines represent the empirical ice flow evidence (drumlins and crag and tails) mapped by Shaw *et al.* (2010); the continuous, thick blue lines show the ice flow pattern interpreted by Kleman *et al.* (2010). Purple triangles show the median calibrated radiocarbon ages in cal ka BP surrounding the Hart Ranges from Dalton *et al.* (2020). The orange hexagons show the optically stimulated luminescence ages from Sacco *et al.* (2017). The locations of the two study sites are shown by the red stars with their weighted-mean exposure ages. The location of Figure 3a and 3b is shown by the green circles. The location of the ice surface profile shown in Figure 7 is given by the black dashed line A–A'. (For interpretation of the references to color in this figure legend, the reader is referred to the web version of this article.)

Ice flow over the Rocky Mountains has thus far remained unconstrained in time, with the ILGM being defined by sub-till radiocarbon ages along the marine-terminating margin (e.g., Clague, *et al.*, 1980; Blaise *et al.*, 1990; Ward *et al.*, 2003; Al-Suwaidi *et al.*, 2006) and by the timing of the early stages of ice retreat along the ice sheet perimeter (Stroeven *et al.*, 2010, 2014; Darvill *et al.*, 2018; Lesnek *et al.*, 2018, 2020; Margold *et al.*, 2019). Here we use in situ produced cosmogenic  $^{10}\text{Be}$  dating on glacial erratic boulders located on two summit peaks on opposite sides of the Hart Ranges of the Rocky Mountains to determine when Cordilleran ice stopped flowing over the mountain range.

## METHODS

### Boulder surface sampling

Glacial erratics located on mountain summits that contain geomorphological evidence of ice flow (e.g., streamlined landforms) were examined (Fig. 3a) and two sites that are accessible by foot were chosen for sampling: one site on the western side (Mount Morfee, 1660 m asl) and one site on the eastern side of the Hart Ranges (Mount Spieker, 1971 m asl). Four boulders were sampled

at each location in order to minimize the impact of choosing a sample with a complex exposure history. Additionally, where possible, erratics with a different lithology to the surrounding bedrock were targeted in order to minimize the chance of cosmogenic nuclide inheritance (Heyman *et al.*, 2011).

Samples from Mount Morfee (RM18-01 to RM18-04) were collected on a flattish, glacially eroded western secondary summit (main summit elevation 1775 m asl) that is situated right at the western mountain front of the Hart Ranges. Sample RM18-01 was collected on the slope west of the secondary summit, samples RM18-02 and RM18-03 were collected directly on the secondary summit, and sample RM18-04 on a col between the secondary summit and the main summit of Mount Morfee (see Fig. 4a–d).

Mount Spieker has a flat, elongated summit surface bordered by steep headwalls of large cirques in all directions. We collected samples RM18-05 to RM18-08 on this summit surface. The boulders from which we collected samples RM18-05 and RM18-06 were situated 60 m and 100 m, respectively, from the eastern rim of the summit, and the boulders of samples RM18-07 and RM18-08 were situated an equal distance between the western and eastern rim of the summit surface. All of the Mount Spieker boulders were perched on the bedrock (see Fig. 4e–h).



**Figure 3.** (color online) Google Earth images of (a) the streamlined features observed on some of the mountain peaks in the Hart Ranges of the Rocky Mountains with a maximum elevation of 1780 m asl and (b) evidence of ice flow through a broad mountain col in the Hart Ranges at an elevation of 1500 m asl. The locations of these figures are shown in Figure 2.

Samples were collected from the top surface of the erratics with a hammer and chisel. Sample locations and elevations were marked with a handheld GPS (~4 m horizontal accuracy), and a clinometer was used to measure the topographic shielding. The selected boulders showed no evidence of denudation and were not covered by moss or other vegetation. In addition, at Mount Morfee, we collected ~30 well-rounded cobbles of glacial drift that littered the surface to determine their provenance in order to test the hypothesis that ice flowed in an easterly direction across the western mountain front.

### Sample preparation and AMS measurements

Measuring the  $^{10}\text{Be}$  concentration in quartz requires several purification steps before the sample can be brought to the accelerator mass spectrometer (AMS) to measure its  $^{10}\text{Be}/^9\text{Be}$  ratio (Gosse and Phillips, 2001). The samples were crushed, sieved, and cleaned with a mixture of HCl and  $\text{H}_2\text{SiF}_6$ . A weighed amount (~0.1 g) of a  $3025 \pm 9$  ppm  $^9\text{Be}$  solution of was added as a carrier to the decontaminated quartz. Beryllium was separated from the solution by successive anionic and cationic resin extractions and precipitations. The final precipitates were dried, heated to 800°C to obtain  $\text{BeO}$ , and mixed with niobium powder. The  $^{10}\text{Be}/^9\text{Be}$  ratio of each

sample was measured at the French 5 MV AMS National Facility ASTER (CEREGE, Aix-en-Provence). The measurements were calibrated directly against STD11 inhouse standard ( $^{10}\text{Be}/^9\text{Be}$  value of  $1.191 \pm 0.013 \times 10^{-11}$ ; Braucher et al., 2015). A process blank was also analyzed and used to subtract  $^{10}\text{Be}$  introduced during target preparation and analysis. This blank ( $^{10}\text{Be}/^9\text{Be} = 2.65 \pm 0.36 \times 10^{-15}$ ) accounts at maximum for 1.6% of the measured ratios.

### $^{10}\text{Be}$ age calculations

The exposure ages were calculated using the online calculator of Balco et al. (2008; version 3.0), with the 'primary' calibration set of Borchers et al. (2016). The ages are reported here using the time-dependent CRONUS LSDn production rate scaling model (Lifton et al., 2014). Individual ages are reported with an external error (reported as  $1\sigma$ ), which accounts for both measurement uncertainties, including uncertainties associated with AMS counting statistics, chemical blank measurements, and AMS internal error (0.5%), as well as uncertainties in the reference nuclide production rate for spallation and the nuclide production rate by muons (Balco et al., 2008). At each site, a weighted mean exposure age was calculated and reported with a weighted mean standard deviation. A chi-squared ( $\chi^2$ ) test was used to examine the distribution of exposure ages at each site (Ward and Wilson, 1978). The 95% critical value for  $\chi^2$  with n-1 degrees of freedom was calculated for each site and compared with the theoretical value ( $\chi^{2\text{crit}}$ ; supplementary material D4). If the calculated value was less than the theoretical value, all ages were used to calculate the mean exposure age. However, if the site did not pass this test, the ages with the largest calculated  $\chi^2$  value were successively excluded until the distribution passed the  $\chi^2$  test (Dunai, 2010). Additionally, following the procedure presented by Blomdin et al. (2016), the reduced chi-squared statistic and the standard deviation to arithmetic mean exposure age ratio was used to determine the approximate scatter in the data and classify the sites as well, moderately, or poorly clustered (see supplementary material D4).

### Processes affecting terrestrial cosmogenic nuclide production rates

A number of processes can affect terrestrial cosmogenic nuclide production rates, including boulder surface denudation, snow and vegetation cover, elevation changes from GIA, and variations in the atmospheric mass distribution over time (Gosse and Phillips, 2001; Jones et al., 2019). There is currently no universal method for addressing and accounting for these processes, and we assessed the effect of each process at our sample sites individually.

We did not correct the apparent exposure ages for surface denudation because most of the boulders consist of highly resistant rocks. The Rocky Mountain range creates a marked topographic barrier to the prevailing westerly winds, causing significant present-day snow cover to occur for eight months of the year at both sample sites. The average snow depth per month exceeds the height of all boulders, therefore, we applied a snow shielding correction to the apparent exposure ages. This snow shielding factor was calculated at each site for each month of the year (monthly snow depth and density data was obtained from nearby manual weather stations; see supplementary material S1; Government of Canada, 2019) and averaged to give an annual snow shielding factor for each sample. The snow depth was calculated individually for each boulder by subtracting the boulder



**Figure 4.** (color online) Photographs of the sampled boulders presented with their apparent exposure ages  $\pm 1\sigma$  external error. (a–d) Boulders RM18-01 to RM18-04 that are located at Mount Morfee. (e–h) Boulders RM18-05 to RM18-08 that are located at Mount Spieker. Boulder RM18-06 is considered an outlier. Note the person and chisel for scale.

height from the monthly snow depth. The snow shielding factor was then calculated according to the exponential attenuation equation for snow shielding presented in Gosse and Phillips (2001, equation 3.76; see supplementary material S1).

The monthly snow depth and density data provide a reasonably good estimate of the present-day snow cover at each site because the data are available over a 50 year period and the weather stations are located at similar elevations and within 50 km of the sample sites. However, our snow cover correction does not account for long term changes in climate over the Holocene, such as the early Holocene thermal maximum (ca. 11.5–8.0 ka) when temperatures were  $\sim 2$ – $4^\circ\text{C}$  warmer than present in western Canada (Pellatt and Mathewes, 1997; Edwards *et al.*, 2008; Gavin *et al.*, 2011; Schwörer *et al.*, 2017). This variation in climate introduces a large uncertainty into our snow cover corrected apparent exposure ages.

The LSDn production rate scaling model was used to determine the specific  $^{10}\text{Be}$  production rate at each of our sample sites as a function of altitude (atmospheric pressure) and latitude.

This scaling model assumes that the atmospheric pressure has remained constant over time. However, at our sample sites, atmospheric pressure has varied due to (1) changes in altitude caused by GIA; and (2) changes in the atmospheric density distribution during the glacial-interglacial cycle due to a range of processes, such as the displacement of atmospheric mass, katabatic winds, and atmospheric cooling (Staiger *et al.*, 2007; Jones *et al.*, 2019). It has been hypothesized that the changes in atmospheric pressure due to GIA might be offset to some degree by the changes in the atmospheric density distribution caused by changes in the climate over time (Staiger *et al.*, 2007; Young *et al.*, 2013), and there has recently been some debate about our ability to properly account for these changes (e.g., Staiger *et al.*, 2007; Jones *et al.*, 2019; Balco, 2020). Here we assess both the time-varying effects of GIA and the changing atmospheric thickness on the  $^{10}\text{Be}$  production rate at our sites since deglaciation.

We used the published relative sea level change ( $\Delta\text{RSL}$ ) data from Lambeck *et al.* (2017; currently the highest resolution GIA model available with a  $0.25 \times 0.25^\circ$  resolution and 500 year

intervals) to determine the average elevation of the sample sites since deglaciation. According to their model, the Mount Morfee and Mount Spieker sites became ice free at 13.0 ka and 13.5 ka, respectively. Therefore, we extracted the  $\Delta\text{RSL}$  value every 500 years since the deglaciation and then calculated the average  $\Delta\text{RSL}$  for the entire period, which results in a change of -62 m at Mount Morfee and -64 m at Mount Spieker (see supplementary material D2). We then corrected the modern elevation of the sample sites by this value before the exposure ages were calculated.

We used the method developed by Cuzzone et al. (2016) for assessing the effect of changing atmospheric thickness on production rates. This method uses the hypsometric equation to calculate the change in atmospheric thickness (m) between the time of deglaciation and the present-day. Simulated variations in surface pressure over time at our field sites and the average temperature since deglaciation were obtained from the output of a coupled atmosphere-ocean general circulation model (simulating global climate at 3 ka time intervals over the last 21 ka; Alder and Hostetler, 2015) and used in the hypsometric equation. Although the temporal (3 ka) and spatial ( $3.75^\circ \times 3.68^\circ$ ) resolution of this model is rather coarse compared with the GIA model, the calculation indicates that the change in elevation due to variations in atmospheric density distribution between 15–0 ka is 3.4 m. This result is consistent with that of Cuzzone et al. (2016) and Ullman et al. (2016), who found that although this correction works in the opposite direction to that of the GIA correction, it is an order of magnitude smaller, and therefore, we excluded it from our overall topographic correction and only account of changes due to GIA.

### Recalculating previously published $^{10}\text{Be}$ ages

All previously published  $^{10}\text{Be}$  ages presented in this paper have been recalculated with the online calculator to ensure they are directly comparable (see supplementary material D3). Where multiple ages are available for a particular site, a weighted mean age has been calculated (excluding outliers identified by the original authors). A snow cover correction was applied only at the Telkwa Range because all the other sites do not receive enough snow cover to require corrections to their exposure ages. A GIA correction was applied to all ages using the method outlined above. The majority of these recalculated ages are younger than the previously published ages; this is coming from the time-dependent CRONUS LSDn production rate scaling scheme.

## RESULTS

The  $^{10}\text{Be}$  exposure ages of each sample are given in Table 1. The four exposure ages obtained from Mount Morfee are well clustered between  $12.0 \pm 0.8$  ka and  $13.0 \pm 1.3$  ka, with a weighted mean age and weighted mean standard deviation of  $12.2 \pm 0.4$  ka (Fig. 5A). At Mount Spieker, sample number RM18-06, with an exposure age of  $20.8 \pm 1.2$  ka, was identified as an outlier and excluded from the weighted mean exposure age calculation for the site based on the results of the  $\chi^2$  calculation (see supplementary material D4). The remaining three samples give moderately clustered exposure ages between  $14.0 \pm 0.9$  ka and  $17.4 \pm 1.0$  ka, with a weighted mean exposure age and weighted mean standard deviation of  $15.6 \pm 0.6$  ka (Fig. 5B).

A number of the cobbles collected from the till at Mount Morfee originated from felsic and mafic intrusive and extrusive

rocks, with the following lithologies identified: rhyolite with alkali feldspar, dacite, tonalite, alkali feldspar granite, gabbro, and basalt. Because the Rocky Mountains and Alberta Plateau (Canadian Prairies) both consist of sedimentary bedrock, these volcanic cobbles were almost certainly sourced from the Northern Cordilleran Volcanic Province, which extends in a north-northwest direction across central British Columbia (Fig. 6). The western provenance of these volcanic cobbles confirms the easterly flow of Cordilleran ice over the Hart Ranges.

## DISCUSSION

### Interpreting the $^{10}\text{Be}$ concentrations

A number of geomorphic processes can cause apparent exposure ages to differ from the true depositional age of a landform (Balco, 2020), and the two main sources of geological uncertainty are nuclide inheritance and incomplete exposure (Heyman et al., 2011). Incomplete exposure results from post-depositional shielding of the sample due to burial and successive exhumation, which causes the apparent exposure age to be younger than the true depositional age. However, we consider it unlikely that the boulders sampled during this study were affected by incomplete exposure because at Mount Morfee, the boulders are too tall to be buried by sediment following deposition (0.65–1.20 m tall), and the majority of boulders at Mount Spieker are resting directly on bedrock.

The four ages from Mount Morfee are well clustered between  $12.0 \pm 0.8$  ka and  $13.0 \pm 1.3$  ka and, therefore, it is unlikely that nuclide inheritance affected the measured  $^{10}\text{Be}$  concentrations within these samples. In contrast, the four exposure ages from Mount Spieker show a larger spread in apparent exposure ages, between  $14.0 \pm 0.9$  ka and  $20.8 \pm 1.2$  ka. It is likely that nuclide inheritance affected the oldest measured sample, RM18-06, because the apparent exposure age of  $20.8 \pm 1.2$  ka is in conflict with the surrounding deglaciation chronology (e.g., Margold et al., 2019; Dalton et al., 2020; Fig. 1). Consequently, this sample is considered an outlier and has been excluded from the weighted mean calculation at Mount Spieker. The remaining three samples are moderately clustered according to the criterion of Blomdin et al. (2016).

### Comparison of the exposure ages with regional deglaciation data

The coalescence of the CIS and LIS east of the Rocky Mountains is now well established (Atkinson et al., 2016; Hartman et al., 2018; Margold et al., 2018), with this study providing further evidence for ice flow over the Rocky Mountains at the ILGM. In contrast, the timing and style of deglaciation in the interior of the ice sheet is very poorly constrained with the mountainous topography thus far impeding the reconstruction of ice sheet-wide glacial retreat patterns. Regionally, deglaciation of the CIS is often characterized by early emergence of mountain peaks due to down-wasting and stagnation of ice in valleys (Fulton, 1967, 1991), however, in some areas, active ice retreat occurred during deglaciation, with active ice retreat of outlet glaciers documented in the Northern Rocky Mountain Foothills (Atkinson et al., 2016) and west of the Rocky Mountain Trench (Margold et al., 2013; Sacco et al., 2017). In the Rocky Mountains, the style and pattern of ice retreat is not well understood and may differ from other areas of the CIS because the mountain range forms a pronounced topographic barrier perpendicular to ice flow. While it is likely

**Table 1.** Location and description of the samples collected at Mount Morfee and Mount Spieker during this study. The uncorrected and snow cover and GIA corrected surface exposure ages are given for the individual samples RM18-01 to RM18-08 as well as the calculated weighted mean exposure age for each sample site. Only the snow cover and GIA corrected exposure ages are referred to in the text.

Sample site	Sample code	Latitude (°N) Longitude (°W)	Elevation (m asl)	Sample thickness (cm)	Boulder height (m)	Lithology (density g/ cm <sup>3</sup> )	Topographic shielding factor	Snow cover shielding factor	<sup>10</sup> Be concentration (atoms/g SiO <sub>2</sub> )	Uncorrected exposure age (ka)	Snow cover corrected exposure age <sup>a</sup> (ka)	GIA corrected exposure age <sup>b</sup> (ka)	Snow cover and GIA corrected exposure age (ka)
<b>Mount Morfee</b>	RM18-01	55.42032 123.07016	1641	2	1.0	Quartzite (2.65)	0.999628	0.924326	195136 ± 7608	10.6 ± 0.7	11.4 ± 0.7	11.1 ± 0.8	12.0 ± 0.8
	RM18-02	55.42313 123.06363	1681	2	0.65	Gneiss (2.70)	1	0.881554	195296 ± 6549	10.2 ± 0.7	11.6 ± 0.7	10.8 ± 0.7	12.2 ± 0.7
	RM18-03	55.42379 123.06308	1669	1	0.70	Gneiss (2.70)	1	0.887465	196956 ± 6333	10.3 ± 0.7	11.6 ± 0.7	10.9 ± 0.7	12.2 ± 0.7
	RM18-04	55.42119 123.05166	1596	2	1.20	Gneiss (2.70)	1	0.94331	206163 ± 17357	11.6 ± 1.2	12.3 ± 1.2	12.2 ± 1.3	13.0 ± 1.3
<b>Weighted mean age of all samples</b>										<b>10.5 ± 0.4</b>	<b>11.6 ± 0.4</b>	<b>11.0 ± 0.4</b>	<b>12.2 ± 0.4</b>
<b>Mount Spieker</b>	RM18-05	55.13156 121.39724	1926	1	0.70	Quartzite (2.65)	1	0.938392	288168 ± 8213	12.5 ± 0.8	13.3 ± 0.8	13.2 ± 0.9	14.0 ± 0.9
	RM18-06	55.13133 121.39766	1925	2	0.50	Quartzite (2.65)	0.999712	0.916157	414377 ± 11169	18.1 ± 1.2	19.8 ± 1.2	19.0 ± 1.2	20.8 ± 1.2
	RM18-07	55.13148 121.39854	1916	2	0.40	Quartzite (2.65)	0.999103	0.904316	306371 ± 10080	13.5 ± 0.9	15.0 ± 0.9	14.2 ± 1.0	15.8 ± 1.0
	RM18-08	55.13159 121.39853	1918	4	0.35	Quartzite (2.65)	0.999545	0.898487	331120 ± 10657	14.8 ± 1.0	16.5 ± 1.0	15.6 ± 1.0	17.4 ± 1.0
<b>Weighted mean age of samples 05, 07 and 08</b>										<b>13.4 ± 0.5</b>	<b>14.7 ± 0.5</b>	<b>14.3 ± 0.6</b>	<b>15.6 ± 0.6</b>

<sup>a</sup>The snow cover correction makes the ages 6.0–13.7% older.

<sup>b</sup>The GIA correction makes the ages 4.7–5.8% older.

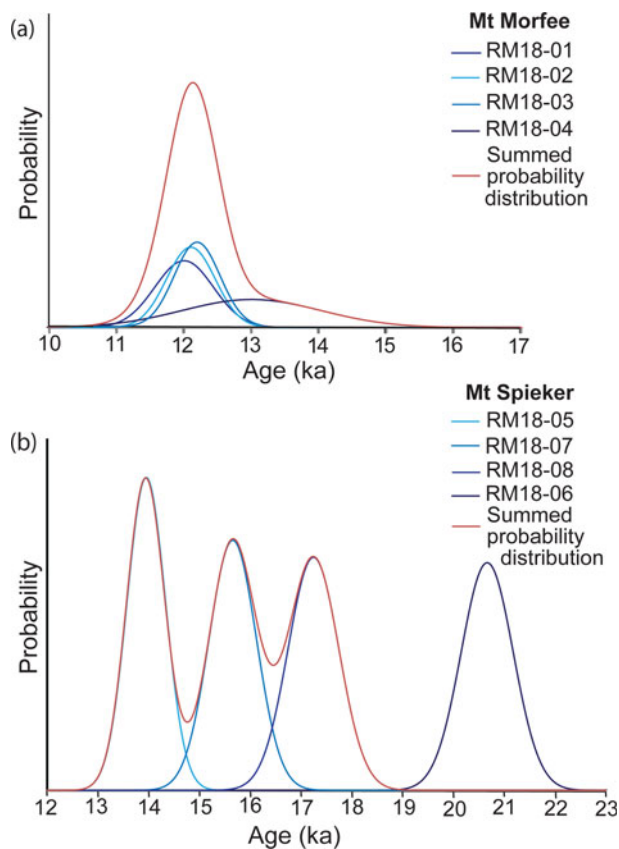


**Figure 5.** (color online) Probability distributions for the apparent exposure ages at (a) Mount Morfee and (b) Mount Spieker. At Mount Spieker, sample RM18-06 has been omitted from the summed probability distribution.

that the mountain summits of Mount Morfee and Mount Spieker emerged from the ice sheet ahead of the retreating ice margin, the relationship between downwasting versus active ice margin retreat remains uncertain (Fig. 7).

The available  $^{36}\text{Cl}$  and  $^{10}\text{Be}$  exposure ages, optically stimulated luminescence (OSL) dates, and radiocarbon dates that relate to the timing of ice retreat across the Hart Ranges are shown in Figures 1 and 2. The timing of deglaciation at Mount Spieker (weighted mean exposure age of  $15.6 \pm 0.6$  ka) is consistent with the age of the Foothills Erratics Train, a group of quartzite boulders scattered linearly along the eastern foothills of the Rocky Mountains (Fig. 1; Jackson et al., 1997; Margold et al., 2019). The deposition of the Foothills Erratics Train at  $15.0 \pm 0.3$  ka ( $n = 12$ ; Margold et al., 2019), immediately preceding the onset of the Bølling warming ( $14.6$ – $12.9$  ka; Rasmussen et al., 2014), marks the beginning of the separation of the Laurentide, Cordilleran, and local mountain ice masses  $\sim 700$  km southeast of the Hart Ranges. However, erratics at elevations of  $\sim 1650$  m asl in the Porcupine Hills (Fig. 1) brought by the last (LGM) ice advance (Jackson et al., 1999) indicate that significant ice surface lowering occurred prior to the deposition of the Foothills Erratics Train and the separation of the ice sheets. We therefore suggest that deglaciation at Mount Spieker could have occurred contemporaneously with the separation of the LIS and CIS farther south.

The weighted mean exposure age at Mount Morfee of  $12.2 \pm 0.4$  ka indicates the CIS extended to the western front of the Rocky Mountains during the Younger Dryas (YD) stadial ( $12.9$ – $11.7$  ka; Rasmussen et al., 2014). This age broadly agrees

with the ice-sheet-scale radiocarbon-based ice margin chronology of Dyke (2004) and Dalton et al. (2020), according to which the eastern margin of the Cordilleran Ice Sheet detached from the western front of the Hart Ranges at some point between  $12.8$  cal ka BP and  $12.1$  cal ka BP. The corrected apparent exposure ages are older than the majority of radiocarbon ages and OSL dates, located immediately west of the Rocky Mountains, with two exceptions highlighted in bold text in Figure 2. The youngest age ( $12.8 \pm 0.15$  cal ka BP, wood, lab. no. GSC-2964; Lowdon and Blake., 1980) is from the upper Fraser River area that likely deglaciated earlier than the Interior Plateau to the northwest, which led to the formation of Glacial Lake Fraser (Clague, 1987; Margold et al., 2013).

There are very few cosmogenic nuclide exposure ages for the interior of the former ice sheet that directly date the deglaciation, with the majority of exposure ages presented by Menounos et al. (2017) for the central sector of the CIS corresponding to a late glacial readvance of smaller mountain glaciers rather than the deglaciation of the CIS. This readvance of cirque glaciers has also been identified in the southern Rocky Mountains (locally termed the Crowfoot Advance; Reasoner et al., 1994; Menounos et al., 2009). However, although the weighted mean exposure age at Mount Morfee falls within the YD stadial, we infer that there is no connection to the regional mountain glacier readvance because there is no geomorphological evidence for it (e.g., readvance moraines) in the Hart Ranges and the sample site is located on a summit peak that does not contain cirques.

Figure 8 shows selected cosmogenic nuclide exposure ages along a west-east transect (shown in Fig. 1) and simulated ice surface profiles along the same transect from Seguinot et al. (2016) and Seguinot (2020). It can be seen that deglaciation at Mount Spieker occurred at roughly the same time as deglaciation along the Pacific Coast, with the ice margin retreating to the mainland coastline by ca. 14 ka (Darvill et al., 2018; Lesnek et al., 2018, 2020). The weighted mean age of  $12.2 \pm 0.4$  ka at Mount Morfee then corresponds to a later stage of deglaciation, being only 1400 years older than that of the Telkwa Range ( $10.8 \pm 0.4$  ka; Margold et al., 2014), which was likely located close to the ice divide. Figure 8 also shows that the cosmogenic exposure ages along the transect broadly fit with the simulated thickness and extent of the CIS at  $20$ – $10$  ka from the numerical model of Seguinot (2020). However, the GRIP ice core temperature data used to drive the Seguinot (2020) simulation induces a dramatic regrowth of the CIS due to the YD cooling, while the empirical evidence to support any such considerable advance is limited.

While our corrected apparent exposure ages from Mount Morfee and Mount Spieker generally fit the surrounding published numerical ages, our poor understanding of the deglacial ice sheet configuration over the Rocky Mountains means our exposure ages cannot be used to constrain the timing of the ice saddle collapse or opening of the ice free corridor east of the Rocky Mountains. However, regardless of the deglaciation style, our exposure ages indicate that the CIS still had a considerable extent during the YD with a surface elevation at the ice divide possibly reaching over 2000 m (Fig. 7). This finding conflicts with the GIA-based ice thickness models of Lambeck et al. (2017) and Peltier et al. (2015), which indicate deglaciation of the Hart Ranges ca. 13.0 ka after the CIS underwent substantial melting, losing up to half its mass, during the Bølling warming (Menounos et al., 2017). A recent paper by Pico et al. (2020), based on gravitationally self-consistent sea level simulations made to fit sea level records over the Bering Strait, has suggested

**Figure 6.** Distribution of intrusive (pink) and extrusive (purple) igneous rocks across part of western North America, overlaid on the ice sheet extent at 22.1 cal ka BP based on the radiocarbon chronology of Dalton *et al.* (2020). The approximate position of the ice divide at the ILGM is shown with thick blue lines; ice flow direction is indicated by thin blue lines (Kleman *et al.*, 2010; Margold *et al.*, 2018, 2019). In the south, the ILGM occurred later than 22.1 cal ka BP, therefore, the maximum ice extent is not shown here. The red stars show the locations of the Mount Spieker and Mount Morfee field sites. This map demonstrates that the volcanic and igneous rocks collected at Mount Morfee were sourced from the west, confirming the easterly ice flow direction over the Rocky Mountains. (For interpretation of the references to color in this figure legend, the reader is referred to the web version of this article.)

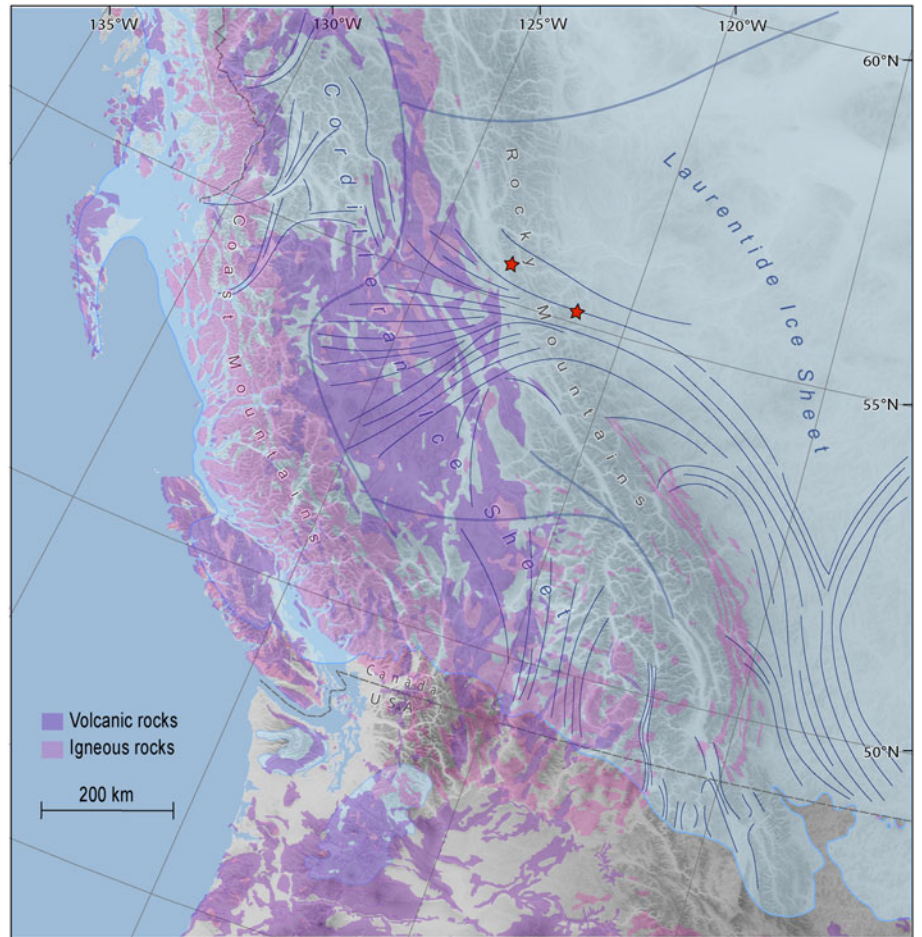


**Figure 7.** Hypothetical ice surface profile of the CIS when the ice margin is located at Mount Morfee, created using the empirical formula derived by Ng *et al.* (2010). We used a length of 400 km that spans 200 km west of Mount Morfee to the approximate position of the ice divide (solid blue line) and 200 km east to an imaginary ice margin (dashed blue line). Using a C coefficient of 3.6, which is similar to the C coefficient of the present-day Greenland Ice Sheet (3.1), the resulting ice surface profile has a height of 1600 m at Mount Morfee. The ice surface profile has been drawn along the flowline A-A' shown in Figure 2. (For interpretation of the references to color in this figure legend, the reader is referred to the web version of this article.)

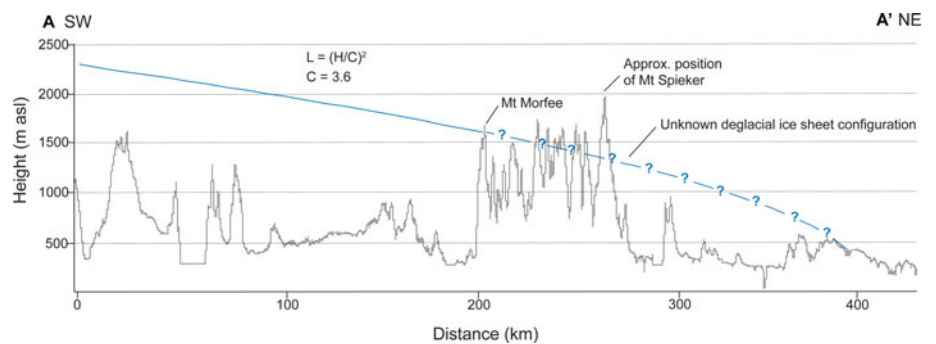
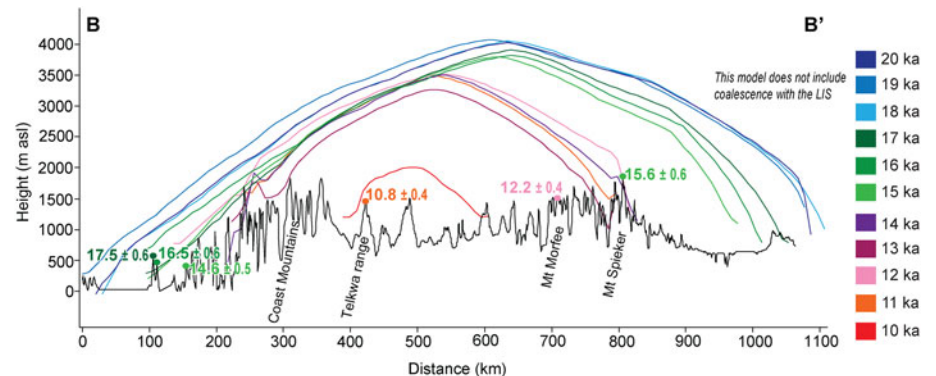


**Figure 8.** (color online) Simulated thickness and extent of the CIS from 20–10 ka from the numerical model of Seguinot (2020) using the GRIP ice core temperature forcing (note the pronounced YD regrowth of the ice sheet at 12 ka that might, at least partially, be an artefact of using the GRIP forcing). The location of the cross profile (B–B') is shown in Figure 1. This cross profile passes through exposure age sample sites at Calvert and King Island (Darvill *et al.*, 2018), Telkwa range (Margold *et al.*, 2014), Mount Morfee (this study), and Mount Spieker (this study). The weighted mean exposure ages from these studies are plotted in their approximate position along the elevation transect.



that this meltwater flux instead happened during the YD stadial (13–11.5 ka).

We therefore suggest that further efforts combining paleogeological reconstructions, based on geomorphological mapping, with numerical dating are needed to understand the deglaciation of the central sector of the CIS and to explain the discrepancy between the numerical ages and ice thickness models. This will allow us to constrain the timing and style of deglaciation in the interior of the ice sheet and to gain a better understanding of how the CIS was affected by the climatic oscillations in the Late Glacial.

## CONCLUSIONS

This study confirms the flow of CIS ice over the Hart Ranges of the Rocky Mountains and uses  $^{10}\text{Be}$  cosmogenic nuclide exposure dating at two sites, one on the western side (Mount Morfee) and one of the eastern side (Mount Spieker) of the Hart Ranges, to determine when ice flow over the mountain range ceased. Samples from our eastern sampling site, Mount Spieker, are moderately clustered in time and yield a weighted mean exposure age of  $15.6 \pm 0.6$  ka, while samples from our western sampling site, Mount Morfee, are well clustered in time and yield a weighted mean exposure age of  $12.2 \pm 0.4$  ka.

Our exposure age at Mount Spieker indicates that the timing of ice retreat at this site occurred roughly contemporaneously with the detachment of the Cordilleran and Laurentide ice sheets to the south. The Hart Ranges might then have been inundated with ice from the west for several thousand years before the CIS retreated from the western front of the mountain range during the YD stadial. The YD timing of ice retreat at Mount Morfee agrees with the available numerical ages that date the deglaciation within the interior of the ice sheet. However, it is difficult to reconcile the age against a number of ice thickness models that predict substantial ice mass loss during the Bølling warming. Further efforts are therefore required to better understand the deglaciation of the central sector of the CIS.

**Supplementary material.** The supplementary material for this article can be found at <https://doi.org/10.1017/qua.2020.122>

**Acknowledgments.** We thank Alessandro Fabbrizio for assistance in identifying the lithologies of the glacial drift hand samples and Tereza Dlabáčková for her assistance with the sample preparation. Chris Darvill is thanked for a useful discussion on the cosmogenic nuclide dating results and Sophie Norris is thanked for discussions about GIA corrections. We thank two anonymous referees and senior editor Nicholas Lancaster for their constructive comments that helped to improve the manuscript.

**Financial support.** This research was supported by the Charles University Grant Agency (GAUK 432119) and the ASTER AMS national facility (CEREGE, Aix-en-Provence) is supported by the INSU/CNRS, the ANR through the “Projets thématiques d’excellence” program for the “Equipements d’excellence” ASTER-CEREGE action and IRD.

## REFERENCES

- Al-Suwaidi, M., Ward, B.C., Wilson, M.C., Hebda, R.J., Nagorsen, D.W., Marshall, D., Ghaleb, B., Wigen, R.J., Enkin, R.J., 2006. Late Wisconsinan Port Eliza cave deposits and their implications for human coastal migration, Vancouver Island, Canada. *Geoarchaeology* **21**, 307–332. <https://doi.org/10.1002/zea.20106>.
- Alder, J.R., Hostetler, S.W., 2015. Global climate simulations at 3000-year intervals for the last 21 000 years with the GENMOM coupled

- atmosphere-ocean model. *Climate of the Past* **11**, 449–471. <https://doi.org/10.5194/cp-11-449-2015>.
- Atkinson, N., Pawley, S., Utting, D.J., 2016. Flow-pattern evolution of the Laurentide and Cordilleran ice sheets across west-central Alberta, Canada: implications for ice sheet growth, retreat and dynamics during the last glacial cycle. *Journal of Quaternary Science* **31**, 753–768. <https://doi.org/10.1002/jqs.2901>.
- Balco, G., 2020. Glacier change and paleoclimate applications of cosmogenic nuclide exposure dating. *Annual Review of Earth and Planetary Sciences* **48**, 21–48. <https://doi.org/10.1146/annurev-earth-081619-052609>.
- Balco, G., Stone, J.O., Lifton, N.A., Dunai, T.J., 2008. A complete and easily accessible means of calculation surface exposure ages or erosion rates from  $^{10}\text{Be}$  and  $^{26}\text{Al}$  measurements. *Quaternary Geochronology* **3**, 174–195. <https://doi.org/10.1016/j.quageo.2007.12.001>.
- Bednarski, J.M., Smith, I.R., 2007. Laurentide and montane glaciation along the Rocky Mountain Foothills of northeastern British Columbia. *Canadian Journal of Earth Sciences* **44**, 445–457. <https://doi.org/10.1139/e06-095>.
- Blaise, B., Clague, J.J., Mathewes, R.W., 1990. Time of maximum Late Wisconsin glaciation, west coast of Canada. *Quaternary Research* **34**, 282–295. [https://doi.org/10.1016/0033-5894\(90\)90041-I](https://doi.org/10.1016/0033-5894(90)90041-I).
- Blomdin, R., Stroeven, A.P., Harbor, J.M., Lifton, N.A., Heyman, J., Gribenski, N., Petrakov, et al., 2016. Evaluating the timing of former glacier expansions in the Tian Shan: A key step towards robust spatial correlations. *Quaternary Science Reviews* **153**, 78–96. <https://doi.org/10.1016/j.quascirev.2016.07.029>.
- Bobrowsky, P., Rutter, N.W., 1992. The Quaternary Geologic History of the Canadian Rocky Mountains. *Géographie physique et Quaternaire* **46**, 5–50. <https://doi.org/10.7202/032887ar>.
- Borchers, B., Marrero, S., Balco, G., Caffee, M., Goehring, B., Lifton, N., Nishiizumi, K., Phillips, F., Schaefer, J., Stone, J., 2016. Geological calibration of spallation production rates in the CRONUS-Earth project. *Quaternary Geochronology* **31**, 188–198. <https://doi.org/10.1016/j.quageo.2015.01.009>.
- Braucher, R., Guillou, V., Bourlès D.L., Arnold M., Aumaitre G., Keddadouche K., Nottoli E., 2015. Preparation of ASTER in-house  $^{10}\text{Be}/^{9}\text{Be}$  standard solutions. *Nuclear Instruments and Methods in Physics Research B* **361**, 335–340. <https://doi.org/10.1016/j.nimb.2015.06.012>.
- Catto, N., Liverman, D.G.E., Bobrowsky, P., Rutter, N., 1996. Laurentide, Cordilleran and montane glaciation in the western peace river—Grande Prairie region, Alberta and British Columbia, Canada. *Quaternary International* **32**, 21–32. [https://doi.org/10.1016/1040-6182\(95\)00061-5](https://doi.org/10.1016/1040-6182(95)00061-5).
- Clague, J.J., 1987. Quaternary stratigraphy and history, Williams Lake, British Columbia. *Canadian Journal of Earth Sciences* **22**, 256–265. <https://doi.org/10.1139/e87-012>.
- Clague, J.J., Armstrong, J.E., Mathewes, W.H., 1980. Advance of the Late Wisconsin Cordilleran Ice Sheet in southern British Columbia since 22,000 Yr B.P. *Quaternary Research* **13**, 322–326. [https://doi.org/10.1016/0033-5894\(80\)90060-5](https://doi.org/10.1016/0033-5894(80)90060-5).
- Cuzzone, J.K., Clark, P.U., Carlson, A.E., Ullman, D.J., Rinterknecht, V.R., Milne, G.A., Lunkka, J.P., Wohlfarth, B., Marcott, S.A., Caffee, M., 2016. Final deglaciation of the Scandinavian Ice Sheet and implications for Holocene global sea-level budget. *Earth and Planetary Science Letters* **448**, 34–41. <http://dx.doi.org/10.1016/j.epsl.2016.05.019>.
- Dalton, A.S., Margold, M., Stokes, C.R., Tarasov, L., Dyke, A.S., Adams, R.S., Allard, S., et al., 2020. An updated radiocarbon-based ice margin chronology for the last deglaciation of the North American Ice Sheet Complex. *Quaternary Science Reviews* **234**, 160223. <https://doi.org/10.1016/j.quascirev.2020.106223>.
- Darvill, C.M., Menounos, B., Goehring, B.M., Lian, O.B., Caffee, M.W., 2018. Retreat of the Western Cordilleran Ice Sheet margin during the last deglaciation. *Geophysical Research Letters* **45**, 9710–9720. <https://doi.org/10.1029/2018GL079419>.
- Dunai, T.J., 2010. *Cosmogenic Nuclides—Principles, Concepts and Applications in the Earth Surface Sciences*. Cambridge University Press, New York.
- Dyke, A.S., 2004. An outline of North American deglaciation with emphasis on central and northern Canada. In: Ehlers, J., Gibbard, P.I. (Eds.), *Quaternary Glaciations—Extent and Chronology, Part II*. Elsevier, Amsterdam, pp. 373–424. [https://doi.org/10.1016/S1571-0866\(04\)80209-4](https://doi.org/10.1016/S1571-0866(04)80209-4).

- Dyke, A.S., Moore, A., Robertson, L., 2003. *Deglaciation of North America: Thirty-two Digital Maps at 1:7,000,000 Scale with Accompanying Digital Chronological Database and One Poster (Two Sheets) with Full Maps Series*. Geological Survey of Canada Open File 1574. <https://doi.org/10.4095/214399>.
- Dyke, A.S., Prest, V.K., 1987. *Paleogeography of northern North America, 18 000–5 000 years ago. Map 1703A, 3 sheets*. Geological Survey of Canada, Ottawa. <https://doi.org/10.4095/133927>.
- Edwards, T.W.D., Birks, S.J., Luckman, B.H., MacDonald, G.M., 2008. Climatic and hydrologic variability during the past millennium in the eastern Rocky Mountains and northern Great Plains of western Canada. *Quaternary Research* **70**, 188–197. <https://doi.org/10.1016/j.yqres.2008.04.013>.
- Fulton, R.J., 1967. Deglaciation studies in Kamloops region, an area of moderate relief, British Columbia. *Geological Survey of Canada, Bulletin* **165**, 1–36. <https://doi.org/10.4095/101467>.
- Fulton, R.J., 1991. A conceptual model for growth and decay of the Cordilleran Ice Sheet. *Géographie physique et Quaternaire* **45**, 281–286. <https://doi.org/10.7202/032875ar>.
- Gavin, D.G., Henderson, A.C.G., Westover, K.S., Fritz, S.C., Walker, I.R., Leng, M.J., Hu, F.S., 2011. Abrupt Holocene climate change and potential response to solar forcing in western Canada. *Quaternary Science Reviews* **30**, 1243–1255. <https://doi.org/10.1016/j.quascirev.2011.03.003>.
- Gosse, J.C., Phillips, F.M., 2001. Terrestrial in situ cosmogenic nuclides: theory and application. *Quaternary Science Reviews* **20**, 1475–1560. [https://doi.org/10.1016/S0277-3791\(00\)00171-2](https://doi.org/10.1016/S0277-3791(00)00171-2).
- Government of Canada, 2019. *Snow Stations Interactive Map*. Available at <https://governmentofbc.maps.arcgis.com/apps/webappviewer/index.html?id=c15768bf73494f5da04b1aac6793bd2e>. [accessed January 17, 2020]
- Hartman, G.M.D., Clague, J.J., Barendregt, R.W., Reyes, A.V., 2018. Late Wisconsinan Cordilleran and Laurentide glaciation of the Peace River Valley east of the Rocky Mountains, British Columbia. *Canadian Journal of Earth Sciences* **55**, 1324–1338. <https://doi.org/10.1139/cjes-2018-0015>.
- Heyman, J., Stroeven, A.P., Harbor, J.M., Caffee, M.W., 2011. Too young or too old: evaluating cosmogenic exposure dating based on an analysis of compiled boulder exposure ages. *Earth and Planetary Science Letters* **302**, 71–80. <https://doi.org/10.1016/j.epsl.2010.11.040>.
- Hickin, A.S., Lian, O.B., Levson, V.M., 2016. Coalescence of late Wisconsinan Cordilleran and Laurentide ice sheets east of the Rocky Mountain Foothills in the Dawson Creek region, northeast British Columbia, Canada. *Quaternary Research* **85**, 409–429. <https://doi.org/10.1016/j.yqres.2016.02.005>.
- Jackson, L.E., Phillips, F.M., Little, E.C., 1999. Cosmogenic  $^{36}\text{Cl}$  dating of the maximum limit of the Laurentide Ice Sheet in south-western Alberta. *Canadian Journal of Earth Sciences* **36**, 1347–1356. <https://doi.org/10.1139/e99-038>.
- Jackson, L.E., Phillips, F.M., Shimamura, K., Little E.C., 1997. Cosmogenic  $^{36}\text{Cl}$  dating of the Foothills erratics train, Alberta, Canada. *Geology* **25**, 195–198. [https://doi.org/10.1130/0091-7613\(1997\)025<0195:CCDOTF>2.3.CO;2](https://doi.org/10.1130/0091-7613(1997)025<0195:CCDOTF>2.3.CO;2).
- Jones, R.S., Whitehorse, P.L., Bentley, M.J., Dalton, A.S., 2019. Impact of glacial isostatic adjustment on cosmogenic surface-exposure dating. *Quaternary Science Reviews* **212**, 206–212. <https://doi.org/10.1016/j.quascirev.2019.03.012>.
- Kleman, J., Jansson, K., De Angelis, H., Stroeven, A.P., Hättestrand, C., Alm, G., Glasser, N., 2010. North American Ice Sheet build-up during the last glacial cycle, 115–21 kyr. *Quaternary Science Reviews* **29**, 2036–2051. <https://doi.org/10.1016/j.quascirev.2010.04.021>.
- Lambeck, K., Purcell, A., Zhao, S., 2017. The North American Late Wisconsinan ice sheet and mantle viscosity from glacial rebound analyses. *Quaternary Science Reviews* **158**, 172–210. <https://doi.org/10.1016/j.quascirev.2016.11.033>.
- Lesnek, A.J., Briner, J.P., Baichtal, J.F., Lyles, A.S., 2020. New constraints on the last deglaciation of the Cordilleran Ice Sheet in coastal Southeast Alaska. *Quaternary Research* **96**, 140–160. <https://doi.org/10.1017/qua.2020.32>.
- Lesnek, A.J., Briner, J.P., Lindqvist, C., Baichtal, J.F., Heaton, T.H., 2018. Deglaciation of the Pacific coastal corridor directly preceded the human colonization of the Americas. *Science Advances* **4**, eaar5040. <https://doi.org/10.1126/sciadv.aar5040>.
- Lifton, N., Sato, T., Dunai, T.J., 2014. Scaling *in situ* cosmogenic nuclide production rates using analytical approximations to atmospheric cosmic-ray fluxes. *Earth and Planetary Science Letters* **386**, 149–160. <https://doi.org/10.1016/j.epsl.2013.10.052>.
- Lowdon, J.A., Blake, W., Jr., 1980. Geological Survey of Canada Radiocarbon Dates XX. *Geological Survey of Canada Paper* 80-7, 1–28. <https://doi.org/10.4095/119073>.
- Margold, M., Gosse, J.C., Hidy, A.J., Woywitka, R.J., Young, J.M., Froese, D., 2019. Beryllium-10 dating of the Foothills Erratics Train in Alberta, Canada, indicates detachment of the Laurentide Ice Sheet from the Rocky Mountains at 15 ka. *Quaternary Research* **92**, 469–482. <https://doi.org/10.1017/qua.2019.10>.
- Margold, M., Jansson, K.N., Kleman, J., Stroeven, A.P., Clague, J.J., 2013. Retreat pattern of the Cordilleran Ice Sheet in central British Columbia at the end of the last glaciation reconstructed from glacial meltwater landforms. *Boreas* **42**, 830–847. <https://doi.org/10.1111/bor.12007>.
- Margold, M., Stokes, C.R., Clark, C.D., 2015b. Ice streams of the Laurentide Ice Sheet: Identification, characteristics and comparison to modern ice sheets. *Earth-Science Reviews* **143**, 117–146. <https://doi.org/10.1016/j.earscirev.2015.01.011>.
- Margold, M., Stokes, C.R., Clark, C.D., 2018. Reconciling records of ice streaming and ice margin retreat to produce a palaeogeographic reconstruction the deglaciation of the Laurentide Ice Sheet. *Quaternary Science Reviews* **189**, 1–30. <https://doi.org/10.1016/j.quascirev.2018.03.013>.
- Margold, M., Stokes, C.R., Clark, C.D., Kleman, J., 2015a. Ice streams in the Laurentide Ice Sheet: a new mapping inventory. *Journal of Maps* **11**, 380–395. <https://doi.org/10.1080/17445647.2014.912036>.
- Margold, M., Stroeven, A.P., Clague, J.J., Heyman, J., 2014. Timing of terminal Pleistocene deglaciation at high elevations in southern central British Columbia constrained by  $^{10}\text{Be}$  exposure dating. *Quaternary Science Reviews* **99**, 193–202. <https://doi.org/10.1016/j.quascirev.2014.06.027>.
- Mathews, W.H., 1978. *Quaternary Stratigraphy and Formology of Charlies Lake (94A) Map Area, British Columbia. Paper 76-20*. Geological Survey of Canada, Ottawa, 25 pp. <https://doi.org/10.4095/104544>.
- Menounos, B., Goehring, B.M., Osborn, G., Margold, M., Ward, B., Bond, J., Clarke, G.K.C., et al., 2017. Cordilleran Ice Sheet mass loss preceded climate reversals near the Pleistocene Termination. *Science* **358**, 781–784. <https://doi.org/10.1126/science.aan3001>.
- Menounos, B., Osborn, G., Clague, J.J., Luckman, B.H., 2009. Latest Pleistocene and Holocene glacier fluctuations in western Canada. *Quaternary Science Reviews* **28**, 2049–2074. <https://doi.org/10.1016/j.quascirev.2008.10.018>.
- Ng, F.S.L., Barr, L.D., Clark, C.D., 2010. Using the surface profiles of modern ice masses to inform palaeo-glacier reconstructions. *Quaternary Science Reviews* **29**, 3240–3255. <https://doi.org/10.1016/j.quascirev.2010.06.045>.
- Pellatt, M.G., Mathewes, R.W., 1997. Holocene tree line and climate change on the Queen Charlotte Islands, Canada. *Quaternary Research* **48**, 88–99. <https://doi.org/10.1006/qres.1997.1903>.
- Peltier, W.R., 2004. Global glacial isostasy and the surface of the ice-age Earth: the ICE-5 G (VM2) model and GRACE. *Annual Reviews of Earth and Planetary Sciences* **32**, 111–149. <https://doi.org/10.1146/annurev.earth.32.082503.144359>.
- Peltier, W.R., Argus, D.F., Drummond, R., 2015. Space geodesy constrains ice age terminal deglaciation: The global ICE-6G\_C (VM5a) model. *Journal of Geophysical Research: Solid Earth* **120**, 450–487. <https://doi.org/10.1002/2014JB011176>.
- Pico, T., Mitrovica, J.X., Mix, A.C., 2020. Sea level fingerprinting of the Bering Strait flooding history detects the source of the Younger Dryas climate event. *Science Advances* **6**, eaay2935. <https://doi.org/10.1126/sciadv.aay2935>.
- Prest, V.K., Grant, D., Rampton, V., 1968. *Glacial Map of Canada. Map 1253A*. Geological Survey of Canada, Department of Energy, Mines and Resources, Ottawa. <https://doi.org/10.4095/108979>.
- Rasmussen, S.O., Bigler, M., Blockley, S.P., Blunier, T., Buchardt, S.L., Clausen, H.B., Cvijanovic, I., et al., 2014. A stratigraphic framework for abrupt climatic changes during the last glacial period based on three synchronized Greenland ice-core records: refining and extending the INTIMATE event stratigraphy. *Quaternary Science Reviews* **106**, 14–28. <https://doi.org/10.1016/j.quascirev.2014.09.007>.

- Reasoner, M.A., Osborn, G., Rutter, N.W., 1994. Age of the Crowfoot advance in the Canadian Rocky Mountains: a glacial event coeval with the Younger Dryas oscillation. *Geology* **22**, 439–442. [https://doi.org/10.1130/0091-7613\(1994\)022<0439:AOTCAI>2.3.CO;2](https://doi.org/10.1130/0091-7613(1994)022<0439:AOTCAI>2.3.CO;2).
- Sacco, D.A., Ward, B.C., Lian, O.B., Maynard, D.E., Geertsema, M., 2017. Quaternary geology of part of the McLeod Lake map area (NTS 093J), central British Columbia: lithostratigraphy, glacial history and chronology. *Canadian Journal of Earth Sciences* **54**, 1063–1084. <https://doi.org/10.1139/cjes-2016-0198>.
- Schwörer, C., Gavin, D.G., Walker, I.R., Hu, F.S., 2017. Holocene tree line changes in the Canadian Cordillera are controlled by climate and topography. *Journal of Biogeography* **44**, 1148–1159. <https://doi.org/10.1111/jbi.12904>.
- Seguinot, J., 2020. *Cordilleran Ice Sheet Glacial Cycle Simulations Continuous Variables [Dataset]*. Zenodo. <http://doi.org/10.5281/zenodo.3606536>. [accessed October 06, 2020]
- Seguinot, J., Rogozhina, I., Stroeven, A.P., Margold, M., Kleman, J., 2016. Numerical simulations of the Cordilleran ice sheet through the last glacial cycle. *The Cryosphere* **10**, 639–664. <https://doi.org/10.5194/tc-10-639-2016>.
- Shaw, J., Sharpe, D., Harris, J., 2010. A flowline map of glaciated Canada based on remote sensing data. *Canadian Journal of Earth Sciences* **47**, 89–101. <https://doi.org/10.1139/E09-068>.
- Staiger, J., Gosse, J., Toracinta, R., Oglesby, B., Fastook, J., Johnson, J.V., 2007. Atmospheric scaling of cosmogenic nuclide production: Climate effect. *Journal of Geophysical Research* **112**, B02205. <https://doi.org/10.1029/2005JB003811>.
- Stroeven, A.P., Fabel, D., Codilean, A.T., Kleman, J., Clague, J.J., Miguens-Rodriguez, M., Xu, S., 2010. Investigating the glacial history of the northern sector of the Cordilleran Ice Sheet with cosmogenic  $^{10}\text{Be}$  concentrations in quartz. *Quaternary Science Reviews* **29**, 3630–3643. <https://doi.org/10.1016/j.quascirev.2010.07.010>.
- Stroeven, A.P., Fabel, D., Margold, M., Clague, J.J., Xu, S., 2014. Investigating absolute chronologies of glacial advances in the NW sector of the Cordilleran Ice Sheet with terrestrial in situ cosmogenic nuclides. *Quaternary Science Reviews* **92**, 429–443. <https://doi.org/10.1016/j.quascirev.2013.09.026>.
- Stumpf, A.J., Broster, B.E., Levson, V.M., 2000. Multiphase flow of the late Wisconsinan Cordilleran ice sheet in western Canada. *GSA Bulletin* **112**, 1850–1863. [https://doi.org/10.1130/0016-7606\(2000\)112<1850:MFOTLW>2.0.CO;2](https://doi.org/10.1130/0016-7606(2000)112<1850:MFOTLW>2.0.CO;2).
- Tarasov, L., Dyke, A.S., Neal, R.M., Peltier, W.R., 2012. A data-calibrated distribution of deglacial chronologies for the North American ice complex from glaciological modeling. *Earth and Planetary Science Letters* **315–316**, 30–40. <https://doi.org/10.1016/j.epsl.2011.09.010>.
- Tarasov, L., Peltier, W.R., 2004. A geophysically constrained large ensemble analysis of the deglacial history of the North American ice-sheet complex. *Quaternary Science Reviews* **23**, 359–388. <https://doi.org/10.1016/j.quascirev.2003.08.004>.
- Ullman, D.J., Carlson, A.E., Hostetler, S.W., Clark, P.U., Cuzzone, J., Milne, G.A., Winsor, K., Caffee, M., 2016. Final Laurentide ice-sheet deglaciation and Holocene climate-sea level change. *Quaternary Science Reviews* **152**, 49–59. <https://doi.org/10.1016/j.quascirev.2016.09.014>.
- Ward, B.C., Wilson, M.C., Nagorsen, D.W., Nelson, D.E., Driver, J.C., Wigen, R.J., 2003. Port Eliza cave: North American West Coast interstadial environment and implications for human migrations. *Quaternary Science Reviews* **22**, 1383–1388. [https://doi.org/10.1016/S0277-3791\(03\)00092-1](https://doi.org/10.1016/S0277-3791(03)00092-1).
- Ward, G.K., Wilson, S.R., 1978. Procedures for comparing and combining radiocarbon age determinations: a critique. *Archaeometry* **20**, 19–31. <https://doi.org/10.1111/j.1475-4754.1978.tb00208.x>.
- Young, N.E., Schaefer, J.M., Briner, J.P., Goehring, B.M., 2013. A  $^{10}\text{Be}$  production-rate calibration for the Arctic. *Journal of Quaternary Science* **28**, 515–526. <https://doi.org/10.1002/jqs.2642>.